



OPEN ACCESS

EDITED BY Karoliina Honkala, University of Jyväskylä, Finland

REVIEWED BY Lang Xu, University of Wisconsin-Madison, United States Alberto Roldan, Cardiff University, United Kingdom

*CORRESPONDENCE
Mesfin Tsige,

☑ mtsige@uakron.edu

SPECIALTY SECTION

This article was submitted to Modelling, Theory and Computational Catalysis, a section of the journal Frontiers in Catalysis

RECEIVED 05 December 2022 ACCEPTED 23 January 2023 PUBLISHED 16 February 2023

CITATION

Guo H, Gerstein EA, Jha KC, Arsano I, Haider MA, Khan TS and Tsige M (2023), Non-reactive facet specific adsorption as a route to remediation of chlorinated organic contaminants. Front. Catal. 3:1116867. doi: 10.3389/fctls.2023.1116867

COPYRIGHT

© 2023 Guo, Gerstein, Jha, Arsano, Haider, Khan and Tsige. This is an open-access article distributed under the terms of the Creative Commons Attribution License (CC BY). The use, distribution or reproduction in other forums is permitted, provided the original author(s) and the copyright owner(s) are credited and that the original publication in this journal is cited, in accordance with accepted academic practice. No use, distribution or reproduction is permitted which does not comply with these terms.

Non-reactive facet specific adsorption as a route to remediation of chlorinated organic contaminants

Hao Guo^{1,2}, Emily A. Gerstein³, Kshitij C. Jha^{1,2}, Iskinder Arsano¹, Mohammad Ali Haider⁴, Tuhin S. Khan⁵ and Mesfin Tsige¹*

¹Department of Polymer Science, The University of Akron, Akron, OH, United States, ²Biena Tech LLC, Akron, OH, United States, ³College of Engineering and Applied Sciences, University of Wisconsin-Milwaukee, Milwaukee, WI, United States, ⁴Renewable Energy and Chemicals Laboratory, Department of Chemical Engineering, Indian Institute of Technology Delhi, New Delhi, India, ⁵Light Stock Processing Division, CSIR—Indian Institute of Petroleum, Dehradun, India

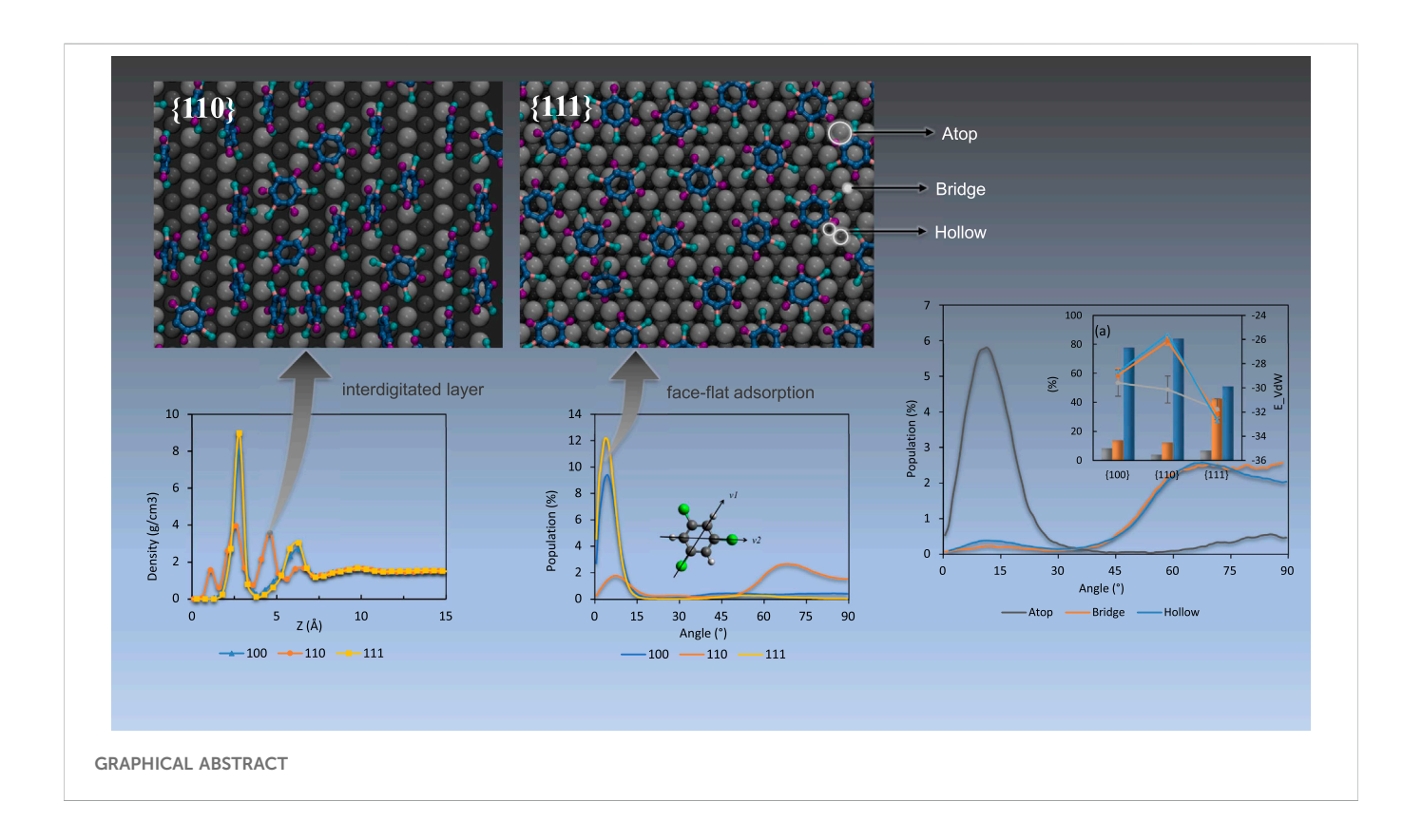
The present work quantifies metal-contaminant interactions between palladium substrates and three salient chlorinated organic contaminants, namely trichloroethylene 1,3,5-trichlorobenzene (TCB), and 3,3',4,4'-tetrachlorobiphenyl (PCB77). Given that Pd is one of the conventional catalytically active materials known for contaminant removal, maximizing catalytic efficiency through optimal adsorption dynamics reduces the cost of remediation of contaminants that are persistent water pollutants chronically affecting public health. Adsorption efficiency analyses from all-atom molecular dynamics (MD) simulations advance the understanding of reaction mechanisms available from density functional theory (DFT) calculations to an extractable feature scale that can fit the parametric design of supported metal catalytic systems and feed into high throughput catalyst selection. Data on residence time, site-specific adsorption, binding energies, packing geometries, orientation profiles, and the effect of adsorbate size show the anomalous behaviour of organic contaminant adsorption on the undercoordinated (110) surface as compared to the (111) and (100) surfaces. The intermolecular interaction within contaminants from molecular dynamics simulation exhibits refreshing results than ordinary single molecule density functional theory calculation. Since complete adsorption and dechlorination is an essential step for chlorinated organic contaminant remediation pathways, the presented profiles provide essential information for designing efficient remediation systems through facet-controlled palladium nanoparticles.

KEYWORDS

chlorinated organic contaminants, palladium nanoparticle, molecular dynamics simulation, adsorption efficiency, catalyst activity

1 Introduction

Chlorinated organic compounds (COCs) are organic compounds containing more than one covalently bonded chlorine atom. COCs usually have low conductivity and long thermal stability and have been extensively used in adhesives, capacitors, etc. Due to their volatility, persistent degradation, and lipophilicity, COCs can quickly spread and accumulate on biological surfaces. The associated health effects include but are not limited to damage to the liver and kidney, congenital disabilities, and reproductive disorders (Brown et al., 1984; Sharma and Bhattacharya, 2017). COCs are by far the most toxic among contaminants broadly



categorized as Persistent Organic Pollutants (POPs) and have geographically widely distributed toxicity. Even COCs incorporated into arctic glaciers *via* water cycles (Wania and Mackay, 1996) may reenter the atmosphere with rising global temperatures, potentially merging with drinking water (Nizzetto et al., 2010). The current study investigates trichloroethylene (TCE), 1,3,5-trichlorobenzene (TCB), and 3,3',4,4'-tetrachlorobiphenyl (PCB77) as three representative COCs among those familiar in water and wastewater. Targeted adsorption of contaminants is critical in water remediation since the nature and range of organic contaminants in different geographies and at different remediation sites may widely differ (Drollette et al., 2015; Essaid et al., 2015; Postigo and Barceló, 2015).

Many methods have been applied to degrade and process COCs. Although biological dechlorination models have previously been reported, such as in the chlorophenol degradation in paper mill bleach (Zheng and Allen, 1996), physical adsorption and catalyst-based methods attract extensive attention because of their high efficiency during treatment. In this regard, zero-valent iron (Hozalski et al., 2001; Clark et al., 2003; Lookman et al., 2004; Parbs et al., 2007; Wang et al., 2018), copper (Hagenmaler et al., 1987; Huang et al., 2011), and zinc (Kim and Carraway, 2003; Bokare et al., 2013) have all been used to reduce chlorinated organics. During the past decade, the use of palladium (Pd) nanoparticles to degrade and process COCs has emerged as a versatile and practical means of removing COCs from water (He et al., 2007; Xu and Bhattacharyya, 2007; Li et al., 2011; Su et al., 2011). This is because Pd is one of the conventional catalytically active materials known for contaminant removal under varieties of conditions (Muftikian et al., 1995; Zhang et al., 1998; Zhang, 2003;

Enache et al., 2006; Ji et al., 2010; Yang et al., 2011; Vijwani and Mukhopadhyay, 2012; Xie et al., 2014; Chen and Ostrom, 2015). The desired catalytic functions may include hydrodechlorination (replacement of chlorine atoms by hydrogen) (Muftikian et al., 1995), hydrogenation and dehydrogenation reactions *via* incorporation into binary alloy membranes (Huang et al., 2011; Mishra et al., 2015; Wang et al., 2018). Jiang and others reported the facet-dependent selectivity of hydrodechlorination reaction on Pd nanoparticles, which facilitate H* generation and phenol desorption on Pd {110} and Pd {111} respectively (Jiang et al., 2020). The high dechlorination activity of Pd Nanoparticles was imputed to significant {111} facets as well as a higher percentage of edge/corner sites by He (He et al., 2016).

The present work focuses on the adsorptive behavior of three commonly occurring Pd facets, namely {111}, {100}, and {110}. Knowledge of interfacial composition and interaction may guide the design of support systems where Pd nanostructures can be loaded, grown, or stabilized for various applications (Cheong et al., 2010; Mishra et al., 2015; Śrebowata et al., 2016; Wang et al., 2018). Relatedly, the effect of palladium support structures has previously been the subject of atomic-level investigations, where density functional theory (DFT) calculations are commonly used. A case in point involves a quantum mechanical study that measured the sensitivity of adsorption of hydrogen molecules on palladium clusters in the presence and absence of carbon support (Warczinski and Hättig, 2019; Warczinski and Hättig, 2020). Unfortunately, a considerable portion of DFT studies focused on single molecule or one molecular cluster, in which the contaminant-contaminant intermolecular interactions ignored. The optimized geometry of an organic containment

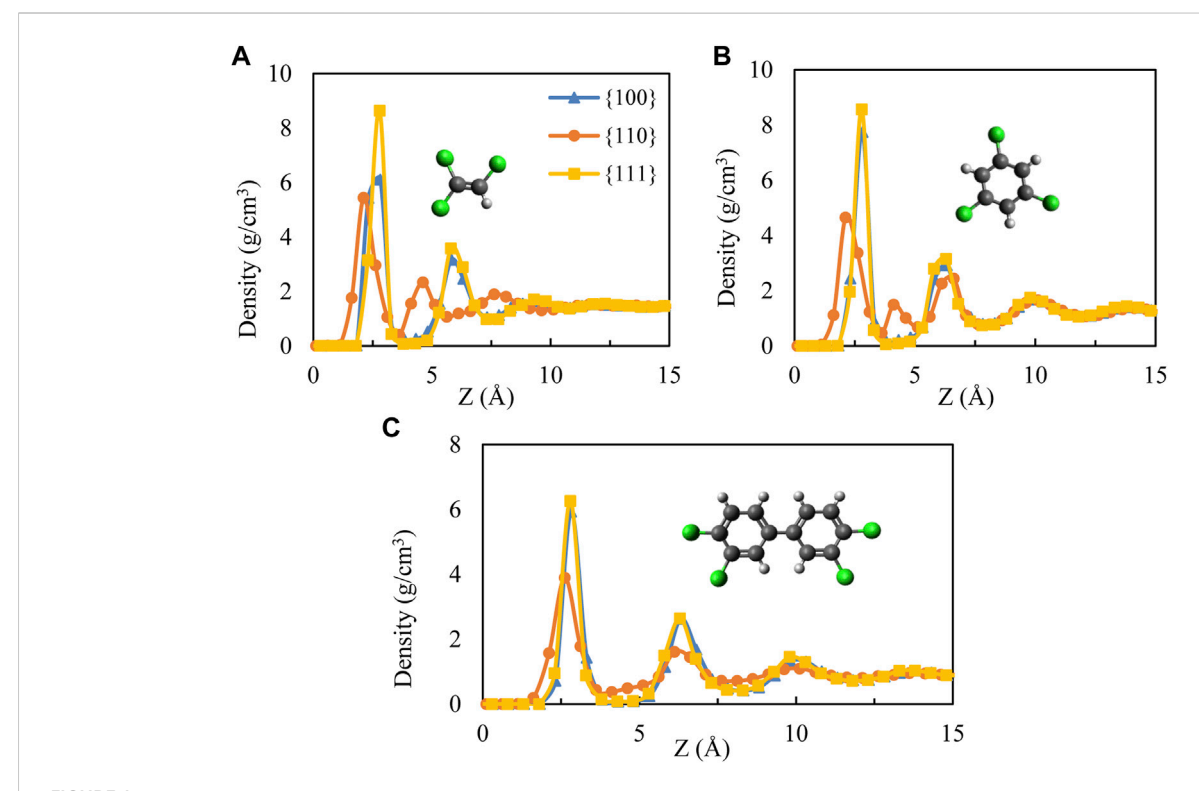


FIGURE 1
Mass density distribution as a function of distance from Pd surfaces for (A) TCE at 230 K, (B) TCB at 360 K and (C) PCB77 at 500 K. The cartoons show the molecular structures of the three organic contaminants studied. The TCB cartoon shows the molecule's symmetrical isomer uniformly used in this study. Chloride, hydrogen, and carbon atoms are represented by green, white, and black, respectively.

molecule reported by DFT calculation may not be successfully applied if an entire layer of containment molecules forming the interface is under study. A larger scale simulation is needed to reliably capture intermolecular effects. Although beyond the scope of the current investigation, there is an additional catalysis impetus for deploying Pd-based water remediation (Lowry and Reinhard, 1999; Enache et al., 2006; Chen et al., 2009; Ji et al., 2010; Tedsree et al., 2011; Yang et al., 2011; Xie et al., 2014).

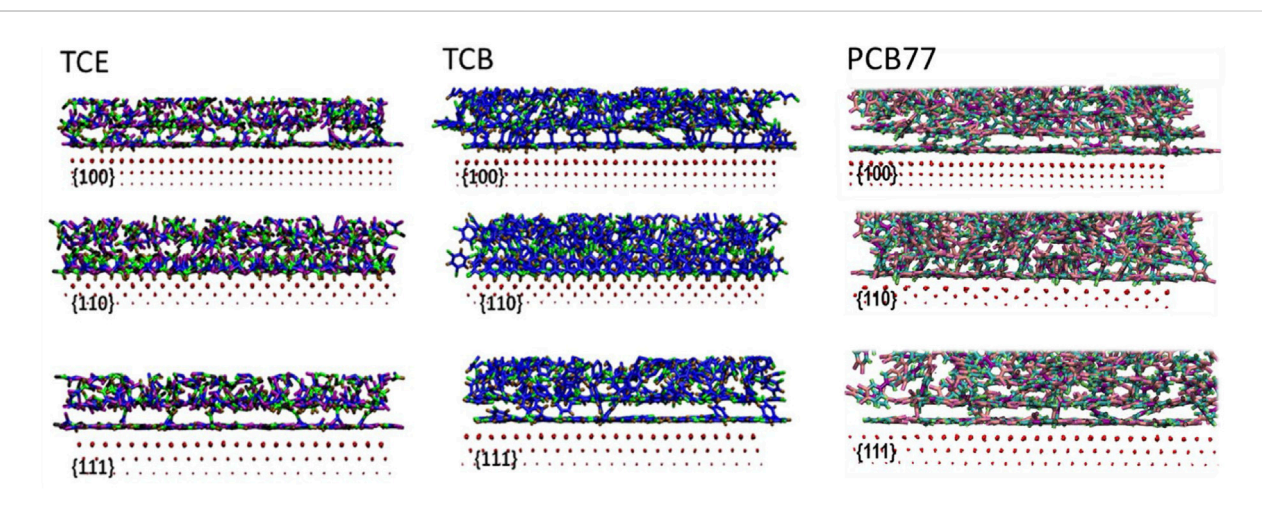
In this study, we provide an assessment on potential effect of catalysis efficiency of the interfacial organization of TCE, TCB, and PCB77 as chosen adsorbates on three different substrates, namely Pd {111}, Pd {110}, and Pd {100} at various liquid temperatures. The reaction mechanisms in our recent work (Shenoy et al., 2021) and others (Lou et al., 2022; Pavloudis et al., 2022) using density functional theory (DFT) have provided an insight into how facet-specific optimal adsorption leads to efficient dechlorination, where molecular orientation will affect dechlorination mechanism and thus affect the catalytic efficiency. To tackle such problems, a system including hundreds of containment molecules using DFT or ab initio MD methods is longed for, but way beyond the capability of simulations. In the current study, to simplify the question into decent freedom, we would like to investigate not merely the single molecule adsorption preference from DFT calculation, but more attention to interface facilitated by a group of molecules. The analysis is provided within the context of adsorption site specificity, dynamics in the adsorption region, and the energy efficiency of surface area use. Our results should be helpful in the design and implementation of Pd nanoparticles for contaminant remediation.

2 Methodology

Molecular dynamics simulations were performed to investigate the non-reactive pure adsorption behavior of organic molecules on planar palladium facets. We used Material Studio software to build three different palladium (Pd) substrates of about 3 nm thickness corresponding to the {100}, {110}, and {111} crystal facets. Dimensions for the Pd supercell were $62.25\times62.25\times31.13~\text{Å}^3$ for {100}, $62.24\times60.52\times31.13~\text{Å}^3$ for {110}, and $55.02\times57.18\times26.95~\text{Å}^3$ for {111}. TCE liquid containing 2,100 molecules was placed on the Pd substrate with a minimum clearance of 3 Å from the top Pd layer to investigate the physical binding between Pd and organics without the presence of water molecule. A similar setup was used for TCB and PCB77 investigations.

All simulations were carried out under the canonical ensemble (NVT) with Nosé–Hoover thermostat using 1 fs timestep. Observation of equilibration stands within around 500 ps of running. A minimum of 3 ns of the additional run was performed beyond the initial equilibration for each system. We selected three temperature values at least 30 K above the experimental melting temperature (Domalski and Hearing, 1996; Van Der Linde et al., 2005) corresponding to each organic compound, which was 230 K–330 K for TCE, 360 K–430 K for TCB, and 500 K for PCB77. The effect of temperature on dynamics, adsorption, and packing has been quantified. While our detailed investigation mainly focuses on the smaller contaminants (TCE and TCB), results for the PCB77 case are also presented when understanding the effect of contaminant molecular size is essential.

All-atom simulations were implemented using LAMMPS (Plimpton, 1995) with Optimized Potentials for Liquid Simulations (OPLS-AA) (Jorgensen et al., 1996) force field parameters, where the



Side view snapshots at the adsorbed state for TCE at 230 K (left panel), TCB at 360 K (middle panel) and PCB77 at 500 K (right panel) for three facets. Only the first three layers of Pd are shown. The size of the Pd atoms correspond to their respective distance from the organic interface. The following color code is used: Pd in red in all figures; (1) left panel: TCE carbon (blue) bonded to two chlorines (violet), the other TCE carbon (cyan) bonded to one chlorine (brown), TCE hydrogen (black); (2) middle panel: TCB carbons (blue), chlorines (cyan), and hydrogens (brown); and (3) right panel: PCB77 biphenyl carbon (purple), PCB77 carbon (peach) bonded to chlorine (pink), PCB77 carbon (cyan) bonded to hydrogen (green).

INTERFACE Force Field (IFF) (Heinz et al., 2008; Heinz et al., 2013) is combined for neutral charged Pd substrates with discrepancy of <0.1% in lattice parameter and <5% in interfacial energies from the reported experiments (Heinz et al., 2008; Kanhaiya et al., 2021). For force field validity testing, bulk simulations were computed for TCE and TCB under the isobaric-isothermal (NPT) ensemble, where densities within 3% of reported experimental values were obtained. With the successful integration and validation of IFF with OPLS-AA FF, the interaction parameters of heavy metals that are used to require dedicated DFT calculations are simplified into Lennard-Jones (LJ) parameters. Though the charge neutrality of the surface may have the drawback of hiding or de-emphasizing potential local electrostatics, the short-range non-bonded interactions captured through LJ are likely to have addressed most of the relevant interactions given the very high aromaticity of all the adsorbates under study. The PPPM method is used for calculating absorbateabsorbate long-range interactions.

Adsorption energies were computed by taking the crosswise non-bonded interactions between the adsorbed first organic layer and the Pd surface. To investigate dynamic properties, mean squared displacement (MSD) and residence time calculations were carried out for molecules that are absorbed on the Pd substrate during the analysis period. Diffusion coefficients were computed from the time-averaged MSD slopes using the Einstein equation. Unless otherwise noted, averages over the last 1 ns were used for the analysis.

3 Results and discussion

3.1 Interface composition and packing

Surface-induced packing has been reported in the literature for several species from simple benzene to oligomers and peptides. Good nanostructure design requires an understanding of the interfacial packing, such as when thermodynamic barriers are readily overcome *via* surfactant induced templating to promote the growth of high-energy corrugated surfaces in Au nanorods (Meena and Sulpizi, 2016).

We begin with mass density profiles of the adsorbed films as a function of distance from the nearest interface with the Pd substrate along the perpendicular direction to the palladium surface (z-axis). Average mass density values were obtained over 0.5 Å bins and are shown in Figure 1 for all contaminant molecules. Note that sthe density profile at the liquid/vapor interface is not included in the figure since the effect of the substrate was not observed beyond ~15 Å.

All systems show similar layering on Pd {100} and {111} facets, significantly differing from what is observed on Pd {110} facet. The non-zero density values relatively very close to the Pd {110} facet for both TCE and TCB (within 1 Å from the interface in the case of TCB) is a result of the organics coming closer to the corrugated {110} surface through the flipped conformation along epitaxial grooves discussed below. In comparison, larger adsorbate-surface separations are detected on the {100} and {111} facets (Figure 1). Furthermore, the intermediate density peak observed around 4 Å on the {110} facet for TCE and TCB is completely absent for the case of PCB77. The density profiles of PCB77 on the three Pd facets are similar, except the density peak values are smaller for the case of {110} facet.

The characteristically diminished interfacial clearance on the Pd {110} surface can be seen in the snapshot views in Figure 2 (middle row). The observation from our recent DFT investigation (Shenoy et al., 2021) is that optimizing adsorption on the three facets is critical to dechlorination and thus provides us the basis to examine packing differences on {100} and {111} facets even though they appear similar from the density profiles. In addition, the first adsorption layers near the {111} facet for TCE and TCB show a high representation of face-flat adsorption exceeding that on {100} (Figure 2). As a direct consequence, much of the organic mass resides at a narrow *z*-axis mark corresponding to the highest first peak compared to adsorption

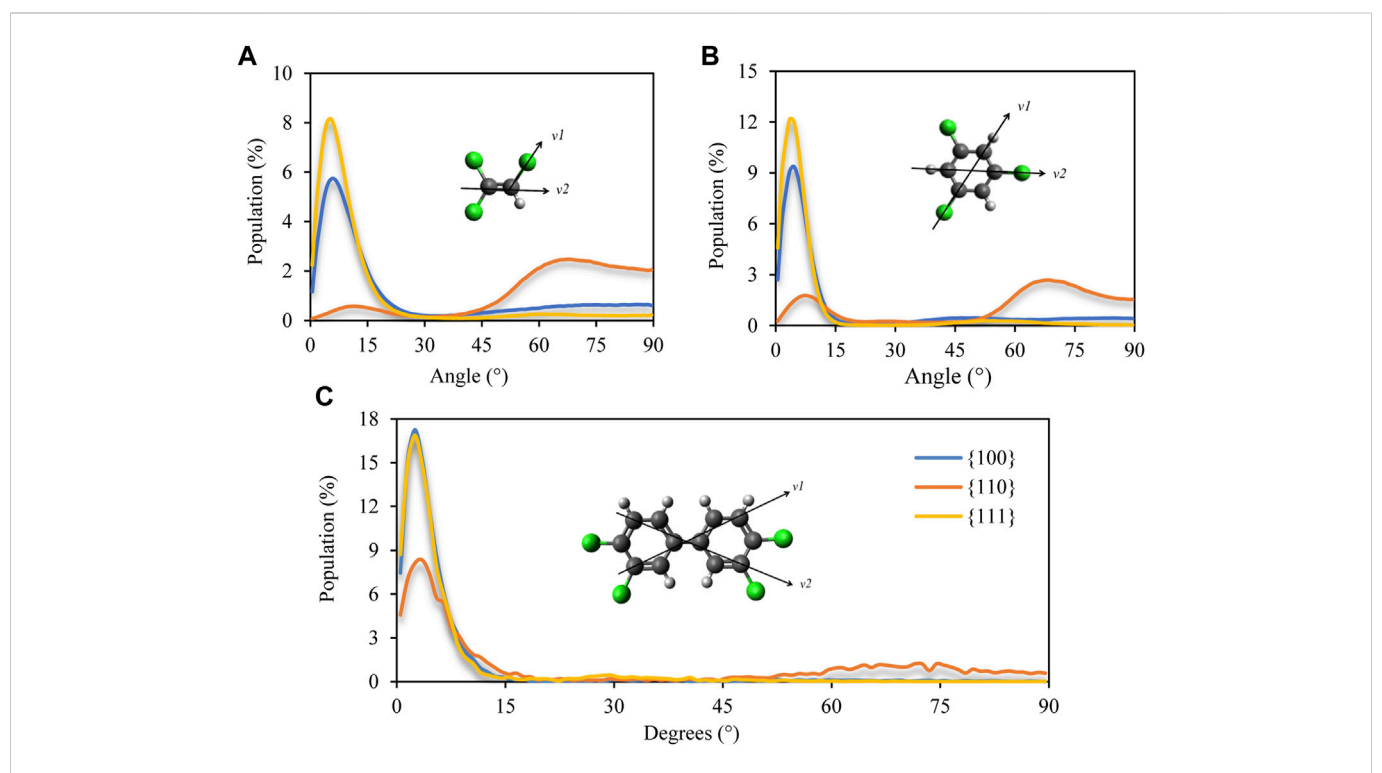


FIGURE 3
Distribution of angles between the molecular face-normal vector (defined by the cross product of vectors v1 and v2) and substrate normal direction. Data for (A) TCE at 230 K, (B) for TCB at 360 K and (C) for PCB77 at 500 K. Zero degree implies average parallel orientation with respect to Pd surface (face-flat) while 90 degrees implies perpendicular (standing) orientation.

on the other two facets (Figure 1). The proportion of face-flat molecules is much smaller on Pd {110} compared to the {100} and {111} facets. While a mixture of face-flat and standing conformations are registered on the {100} and {110} surfaces, a predominantly standing conformation is attained on the {110} surface by both TCE and TCB. It is important to note that the subtle difference between {100} and {111} that is visually apparent here from the MD simulations would be extremely challenging to observe through DFT calculations because of the large number of atoms involved. PCB77, however, shows a similar face-flat adsorption on both {100} and {111} facets. As for the catalytic efficiency, face-flat adsorption is preferred for a single molecule since it makes all chloride atoms closest to Pd directly which could be regarded as active sites for hydrodechlorination reaction. On the contrary, standing geometry could make the best of Pd substrate area but generally provide less (1 or 2) active chloride atoms.

Distinctive for the $\{110\}$ facet of TCE and TCB, at least two mass density peaks appear within $z\sim 5$ Å (Figure 1) from the interface because of an overlapping layer of interdigitated packing conformation of the organic molecules. The overlap appears more pronounced for the TCE molecules. The interdigitated mass density peaks in the vicinity of Pd $\{100\}$ and Pd $\{111\}$, on the other hand, are displaced further from the surfaces and are the result of a propagating layering effect arising from the relative conformational uniformity compared to the Pd $\{110\}$ surface. In keeping with the mass density profiles, trajectory visualizations confirm that adsorbed molecules in the vicinity of the Pd $\{110\}$ remain within 5 Å from the exposed surface. This boundary is therefore used for all systems to delineate the adsorption region in

all subsequent centers of mass-based orientation, energetic and molecular mobility calculations, and comparisons.

The planar molecular structure of all contaminant compounds was taken advantage to devise an orientation descriptor in the form of a face-normal vector defined by the cross product of two vectors on the molecular plane (see cartoon insets in Figure 3). To quantify the observation garnered from the visualization in Figure 2, the angle distribution between the z-axis (direction normal to exposed Pd surface) and the molecular face-normal vector was calculated. Figure 3 corroborates the observations thus far: a narrow distribution of angles between 0 and 15 degrees is registered on Pd {100} and Pd {111} surfaces. In contrast, for TCE and TCB on the Pd {110} facet, most adsorbed molecules attain a preferentially standing configuration on the substrate (angle >45°) with a highly reduced face-flat population. The fact that the slightly bigger contaminant molecules, PCB77, are mostly adsorbed with faceflat orientation regardless of Pd facet type (Figure 3C) is a clear indication that the size and shape of the containment molecules may have a significant effect on their packing and orientation behavior near Pd nanoparticles.

Figure 4 shows how the contaminant molecules' first layer is ordered near Pd substrate. For TCE molecules, the placement of the double bond with respect to the Pd surface can be tracked to determine the packing coordination for the first layer. Similarly, for TCB and PCB77, the placement of the aromatic rings can be tracked to determine the soft networks in the first and subsequent adsorbed layers. TCE and TCB show a distinct horizontal spatial hexagonal packing on Pd {100} and Pd {111} facets, while PCB77 does not show any regular ordered packing in any of the facets. Further,

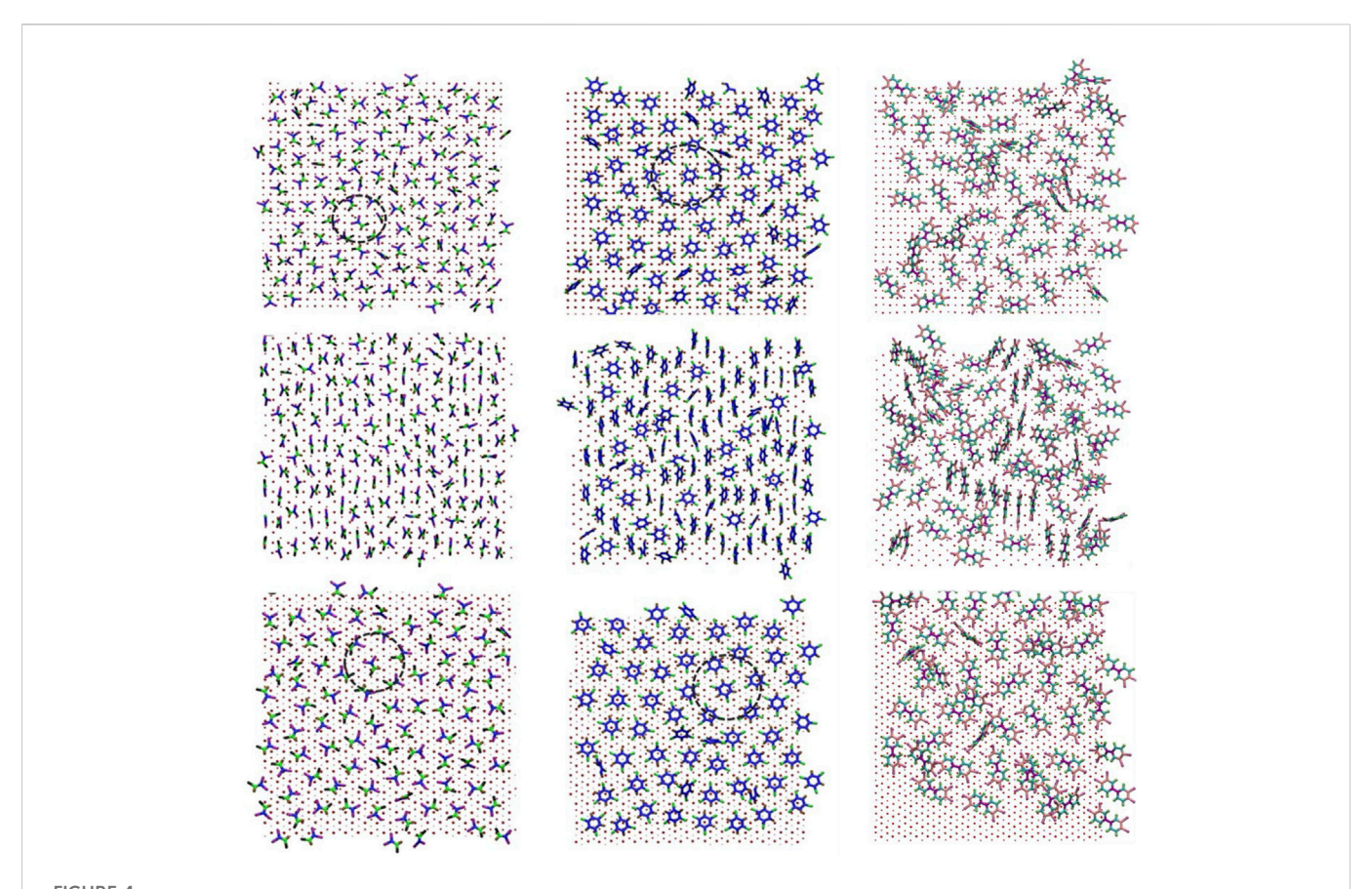
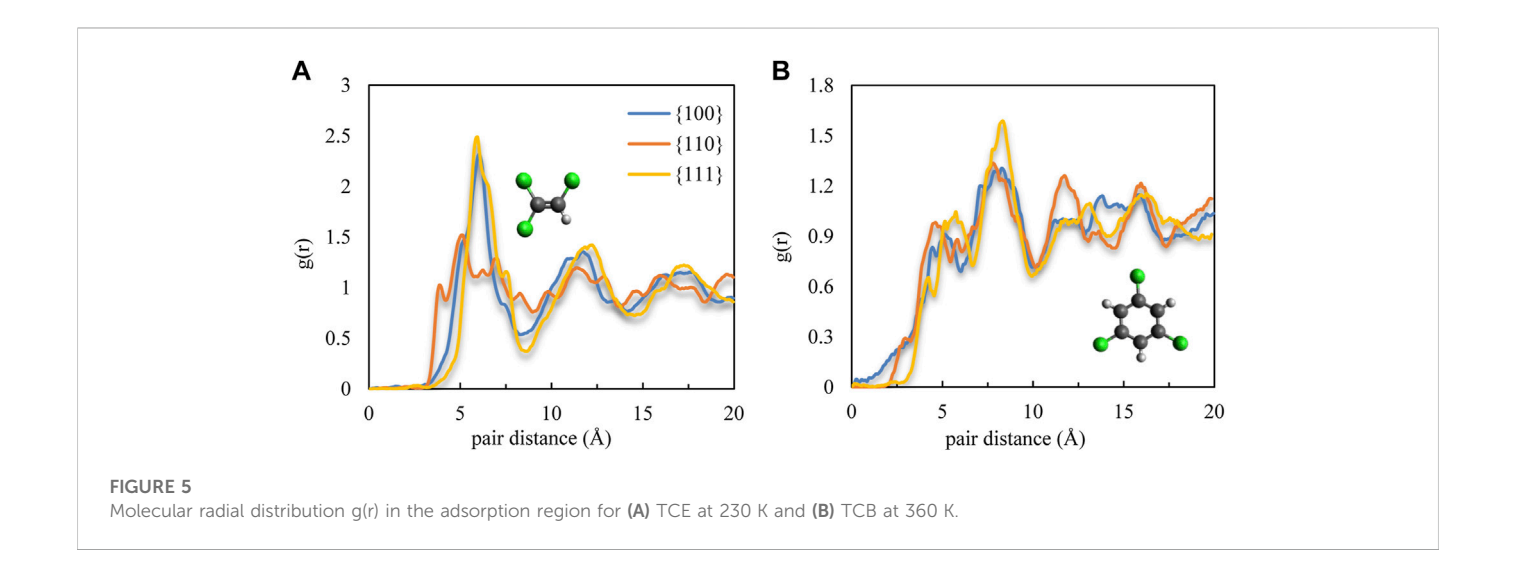


FIGURE 4
Top view snapshot of packing of adsorbate layers for TCE at 230 K (left column), TCB at 360 K (middle column) and PCB77 at 500 K (right column) for three facets: Pd {100} (top row) Pd {110} (middle row) and Pd {111} (bottom row). The color scheme is the same as in Figure 2. Black circles represent example patches of hexagonal packing. Enlarged snapshots for PCB77 molecules are also shown in Supplementary Figure S3.



dechlorination of TCE happens through the Langmuir–Hinshelwood mechanism, in which all adsorbates bind prior to dechlorination (Shenoy et al., 2021). As done in this work, a detailed analysis of the binding of TCE and TCB on various facets should guide the hydrodechlorination investigation of these molecules on Pd surfaces.

We contrast these observations with the behavior of PCB77 (Figure 3C), where this dual-ring molecule prefers an even greater face-flat alignment with the substrate than the single-ring TCB driven by the increased aromatic-aromatic interactions between PCB77 molecules (see Supplementary Figure S3).

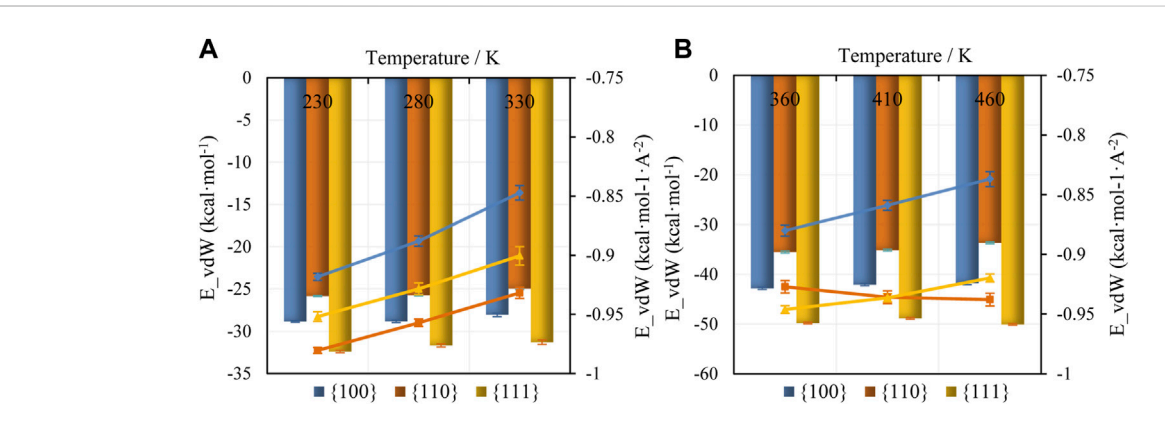
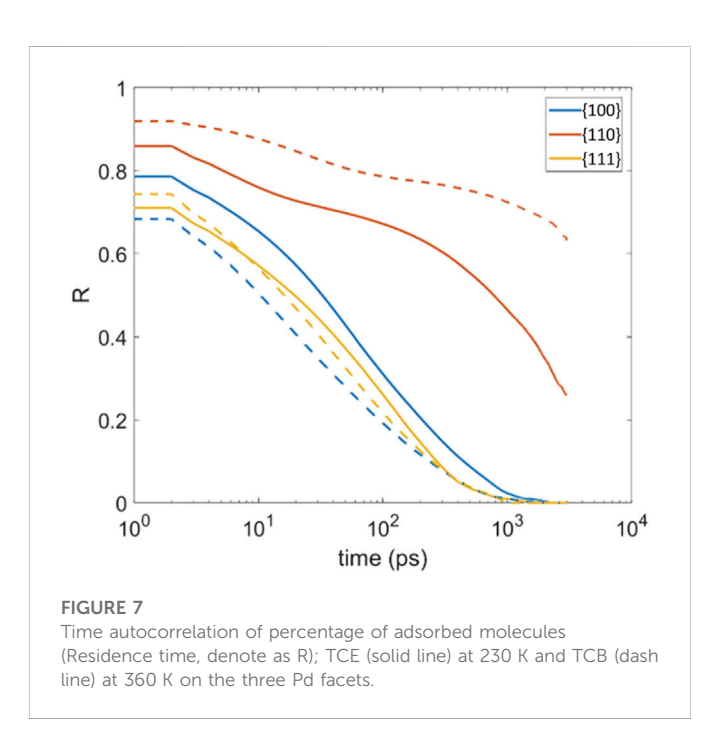


FIGURE 6
Adsorption Energy in the adsorption region for (A) TCE and (B) TCB molecules for different facets and temperatures. Values are shown in units per molecule (bar chart, left vertical axis) and units per unit area (line plot, right vertical axis).

To quantify the distinctive horizontal packing visualized for TCE and TCB, we sought to measure the molecular distribution in the first adsorbed monolayer via radial distribution function (RDF), g(r), where the x- and y-coordinates are used for a two-dimensional (surface) treatment. The calculations track the spatial center of the C=C double bond for TCE and the ring center for TCB (Figure 5). The RDF results show a visible ordering of TCE molecules on top of both Pd {100} and Pd {111} where the position of the first peak at around 6 Å (Figure 5A) corresponds to the first nearest intermolecular distance. The Pd {111} surface, with the highest uniformity of faceflat adsorption, showed a distinctly visible structure, also around 6 Å, for TCB (Figure 5A). In comparison, the g(r) of TCE on the Pd {110} facet barely indicates the formation of a well-ordered structure (Figure 5A). This lack of apparent packing behavior arose from the formation of the interdigitated layer characterized, as shown in the preceding discussions, by a mixture of face-flat and standing conformations. However, for the case of TCB on the Pd {110} facet (Figure 5B), the epitaxial grooves induce the ordering of a large number of standing TCB molecules, and as a result, several peaks are observed in the g(r). In contrast, the small number of standing TCB molecules on the Pd {100} facet disrupts the primary hexagonal packing ordering of the face-flat laying TCB molecules (Figure 4) resulting in a decreased positional order with fewer g(r) peaks (Figure 5B).

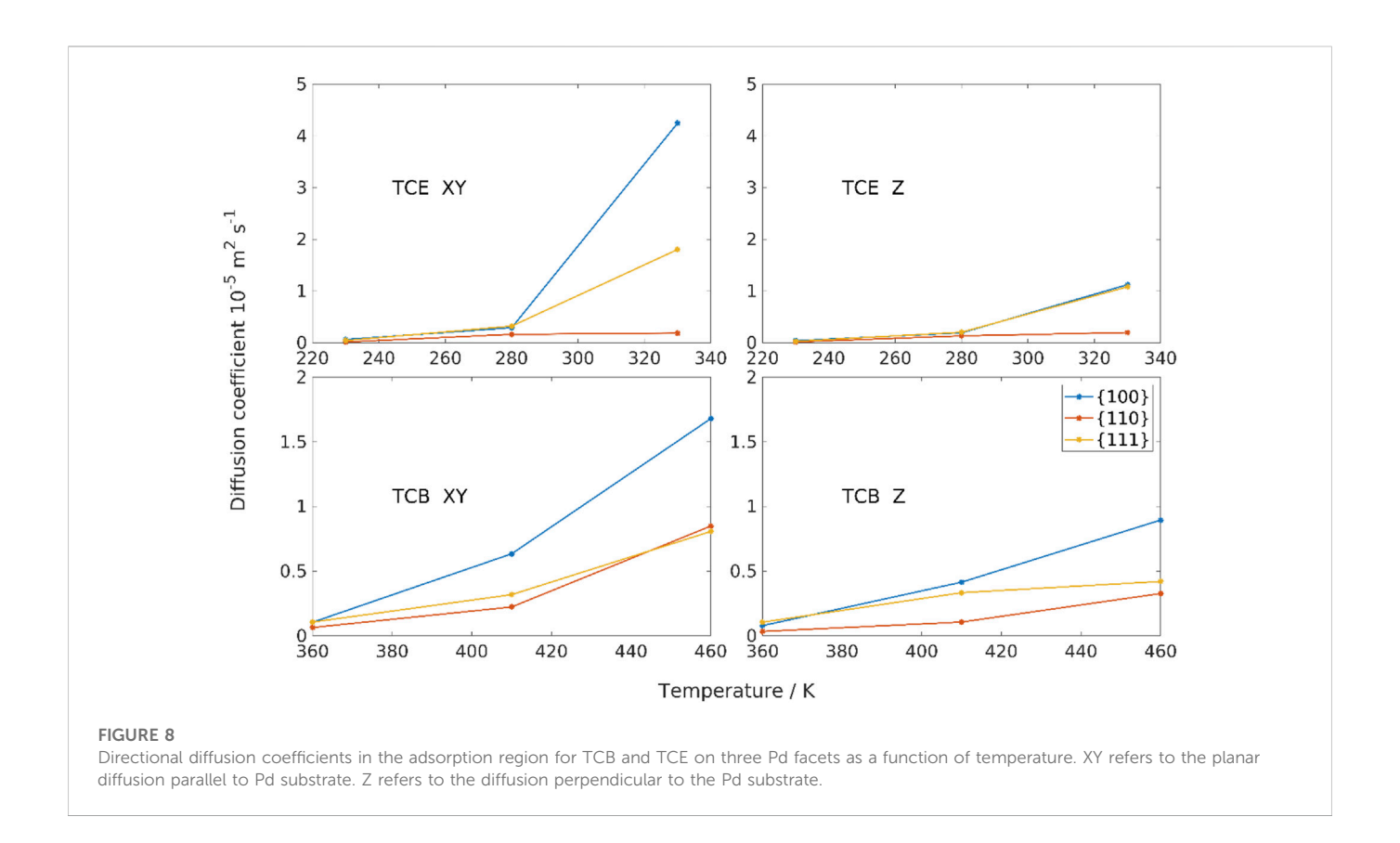
3.2 Thermodynamic properties

Adsorption energies have been computed for the various facets and molecular types in the adsorption region (within 5 Å of the facet surface). A focus on this region is warranted since it accounts for over 90% of adsorption energy in the current study. Temperature dependencies are shown in Supplementary Table S1; Figure 6, where larger negative magnitudes indicate stronger surface affinity. While the binding energy of TCE and TCB for the three facets at different temperatures are shown in Figure 6, the binding energy of PCB77 for the three facets at 500 K is shown in Supplementary Figure S5, S6. Binding energies in Figure 6 are plotted as bar charts in units per molecule. Corresponding per-unit area values are plotted as lines. These two energy formulations provide complementary information.



The per-molecule energy values reflect the adsorption quality dictated by each molecule's interaction strength with the metal surfaces. On the other hand, the per-unit area energy values indicate surface area utilization by the population of adsorbates. Energy differences across systems arising from adsorption region size variation are minimal (molecular counts in the adsorption region are provided in Supplementary Figure S1 of Supplementary Information).

The average per molecule adsorption behavior (Figure 6, bar graphs) uniformly follows the surface affinity hierarchy Pd $\{110\}$ < Pd $\{100\}$ < Pd $\{111\}$ across all systems and temperatures, mirroring the trend for proportion of face-flat adsorbates on top of each substrate. The group adsorption behavior is most clearly seen in the per-unit area energy values (Figure 6, line plot). First, the interdigitation on the $\{110\}$ surface provides the strongest binding, followed by the energy from the predominantly face-flat adsorption on the $\{111\}$ surface. The trend holds even with an expected increase in molecular mobility as



the temperature is elevated (Figure 6A line plot). Second, these same two facets proved to be the most binding (Figure 6B line plot) during TCB adsorption with the following noteworthy difference from TCE adsorption. At the lowest studied liquid, TCB temperature of 360 K face-flat adsorption on the {111} surface provided a dominant energy effect. However, an increase in temperature resulted in a crossover where energy dominance shifts to the interdigitated adsorption on the {110} surface (Figure 6B line plot). PCB77 follows almost similar per molecule surface affinity hierarchy of Pd {110} < Pd {111} \sim Pd {100} (Supplementary Figure S5). Nevertheless, the same surface affinity hierarchy is observed for both per-molecule and per-unit-area on account of the lack of interdigitation confirmation.

All told while face-flat adsorption (Pd {111}, likely majorly driven by aromatic forces in the case of TCB and PCB77) enhances molecule-substrate interaction for more available active chloride atoms. When they appear, standing molecules should be sufficiently interspersed (Pd {110}) in the mix for an energyefficient surface utilization. The intermediate scenario (Pd {100}), where a relatively limited number of standing adsorbates exist among a preponderance of face-flat molecules, is the least energetically favored for the case of TCE and TCB. We hypothesize that the catalytic activity is a trade-off process between 1) maximizing active chloride utilization via an increased face-flat packing and 2) maximizing amount of adsorption via an increased count of molecules with standing geometry. We calculated the number of active chloride molecules and corresponding binding energy per chloride, reported in Supporting Information .Supplementary Table S4 The binding energy per chloride ($E_{b/Cl}$) follows {111} > {110} > {100}. The high binding energy on {111} facet is correlated with the high molecular size to TCB and PCB77 molecules involved in aromatic interaction. The relatively high dechlorination of phenol pollutants on Pd {111} is consistent with previous experimental results (He et al., 2016; Jiang et al., 2020).

It is important to note that first principles investigation using density functional theory (DFT) usually consider the adsorption properties of a single molecule on a small representative surface area of a catalyst and lack accurate estimation of dispersion interactions. Our recent DFT calculations of the adsorption properties of a single TCE molecule on Pd {111}, Pd {100}, Pd {211}, and Pd {110} have shown that the binding energy of TCE is the highest on the Pd {110} facet (Shenoy et al., 2021), which is consistent with our per-area but different from per-molecule result reported in Figure 6A. To make a direct comparison with the DFT results, the binding energies of a single TCE molecule on Pd {111}, Pd {100}, and Pd {110} facets were determined through MD simulations. The binding energy results from the simulations are -25.6, -29.7, and -26.3 kCal/mol for TCE on Pd {100}, Pd {110} and Pd {111}, respectively. A comparison of results between single TCE using MD and DFT is shown in Supplementary Figure S5. Both DFT and MD results clearly confirm that a single TCE molecule has the highest binding energy on the Pd {110} compared to the other Pd surfaces. Dispersion interactions included in classical force fields accurately estimate the behavior in packed geometries, which is not obtainable at the length and time scales through DFT, even when dispersion corrections are included.

Given that the adsorption behavior is dictated by the presence of other organic molecules and the interaction among them, the per area

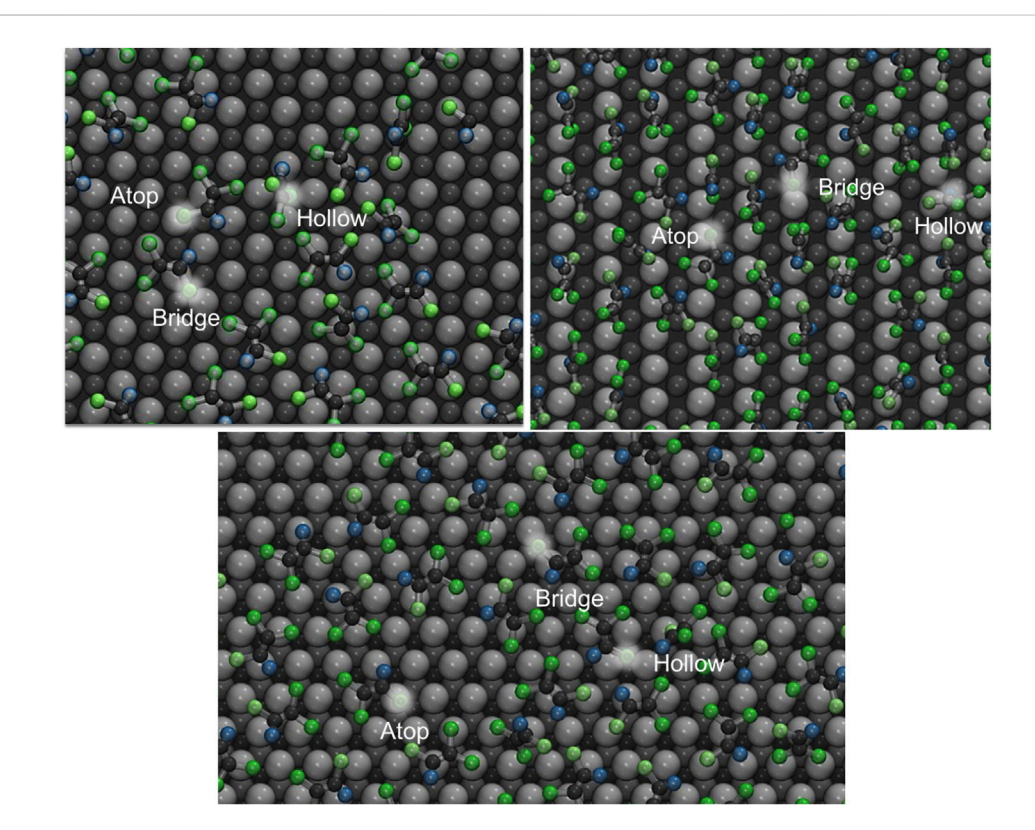


FIGURE 9
Scheme of TCE adsorption on the different adsorption sites on the Pd {100} facet (top left), {110} (top right), {111} (bottom) at 230 K. The bright spots indicate the lowest z-coordinates used to assign adsorption site. Pd substrate coloring is based on the distance from the interface, namely light grey (first Pd layer), dark grey (second Pd layer), black (third Pd layer only for {111}). Hydrogen, chloride, and carbon atoms are represented by blue, green and matte black respectively.

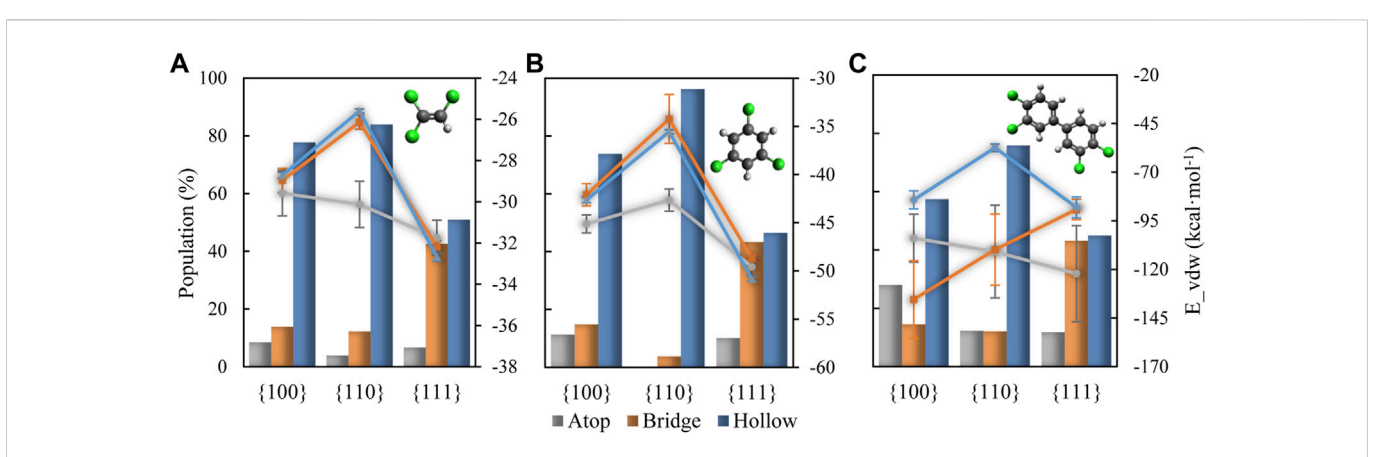


FIGURE 10
Proportion of adsorbed molecules adsorbed on the different sites for (A) TCE at 230 K, (B) TCB at 360 K and (C) PCB77 at 500 K shown in bar chart and with left vertical axis. Corresponding binding energy values are shown in solid lines and with right vertical axis.

binding energy reported in Figure 6 should be more informative than the binding energy of a single molecule in determining the efficacy of a Pd surface for contaminant removal. The results reported here merely consider Van de Waals binding energy between Pd and organic molecules. The energy contribution from electrons hybridization and activation energy barriers for different molecular orientation on different facets should be considered in determining the efficacy of a Pd surface for contaminant removal.

3.3 Dynamics of TCE and TCB molecules on Pd surfaces

Surface residence, total diffusion, and directional diffusion of TCE and TCB molecules in the adsorption region were analyzed as a function of temperature for the three different facets. All dynamic calculations have been done using time averaging. The dynamics of PCB77 molecules in the adsorption region are observed to be very slow

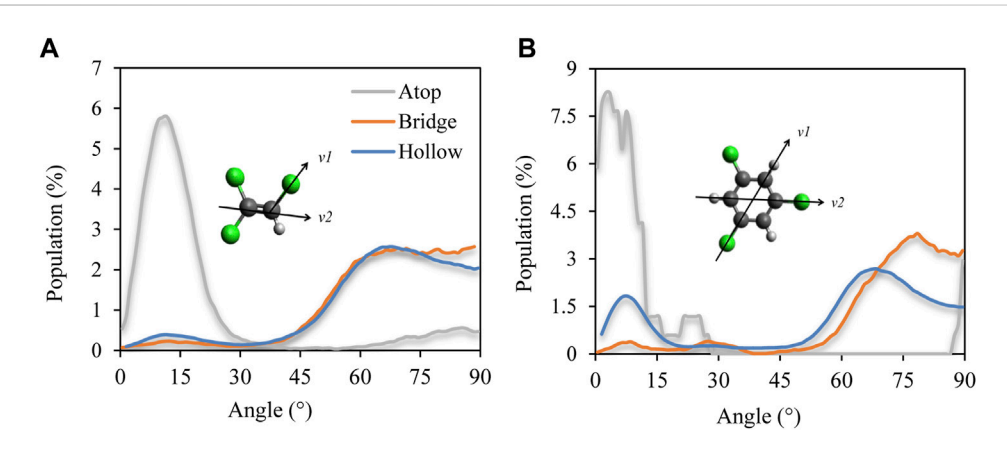


FIGURE 11
Adsorption site decomposition of distribution of angles between the molecular face-normal vector (defined by the cross product of vectors v1 and v2) and the surface perpendicular, or z-axis, for Pd {110} as a representative case. Data for (A) TCE at 230 K and (B) for TCB at 360 K. Zero degree implies average parallel orientation with respect to Pd surface while 90 degrees implies perpendicular (standing) orientation.

compared with those of TCE and TCB and are not discussed here since a much longer simulation time is needed to reach a meaningful conclusion about their dynamics.

The surface residence was determined as time autocorrelation for each time step in the last several nanoseconds of the production run. The resulting curves for select temperatures are illustrated in Figure 7 based on the relation: $R(t) = \frac{1}{N_h} \sum_{i=1}^{N_h} [\theta_i(0)\theta_i(t)]$. Here, N_h is adsorbed molecule count at reference time, and $\theta_i(t)$ is a binary descriptor specifying if the molecule of interest is inside the adsorption shell $(\theta_i(t) = 1)$ or has migrated out $(\theta_i(t) = 0)$ at a given time t.

While a full decorrelation would require orders of magnitude longer simulations, we note that the rate at which the autocorrelation curves decay starting from a value of one largely influences the area under each curve, when fully extrapolated, equals residence time. Figure 7 shows that the {110} has the highest adsorbate retention capability than the other two facets for both TCE and TCB molecules. The adsorbate retention time shows {110} > {100} \approx {111}. The strongly interdigitated packing conformation on the {110} facet seems to limit the mobility of the molecules on this facet. Further, TCB molecules tend to reside relatively more than their TCE counterparts for each substrate type.

The relatively high adsorbate retention time of the Pd $\{110\}$ facet is well correlated with a suppressed mobility of the molecules on this facet, as shown in Figure 8. This behavior is analogous to previously studied haloalkane adsorption on surfaces like graphite and α -quartz (Leuty et al., 2009; Leuty and Tsige, 2010; Leuty and Tsige, 2011), where the melting temperature at the adsorbed interface shifts by several degrees above the bulk value. At high temperatures, the $\{100\}$ facet entertains the highest directional mobility of adsorbates among all facets (Figure 8). Generally, surface-perpendicular diffusion is much smaller than lateral diffusion favorably indicating that adsorbed molecules are more likely to remain in the adsorption region than to migrate away from the interface.

3.4 Adsorption site specificity

To illustrate the detailed nature of local packing and simplify the quantification of the catalytic efficiency of containment removal, the palladium surfaces were divided into three different site types (see representative visualization in Figure 9). We assume molecules

belonging to the same site should share a similar activation energy, reaction when energy and energy undergoing hydrodechlorination reaction. Under that condition, the energy calculation of entire system could be simplified into adsorption energy at each of the three sites. The adsorption site assigning strategy follows: The top layer Pd atoms are identified as 'atop' sites. Spaces between adjacent atop sites are considered 'bridge' sites. Pd atoms in the second (hcp hollow) and third (fcc hollow) layers are all named 'hollow' sites. The lowest z-coordinate of each organic molecule was projected on XY plane, and the distances to nearest Pd sites were determined. The site type with the shortest distance among three types was used to determine the adsorption type of the COC molecule in question. The decomposition of adsorption energies and angle distributions based on the adsorption site are given in Figures 10, 11. The energy values are tabulated in Supplementary Table S2, and substrate site schemes are shown in Supplementary Figures S1, S2.

As shown in Figure 10, adsorption at hollow sites is highly represented on {100} and {110} facets for the three organics. On the {111} facet, both hollow and bridge sites serve as likely adsorption sites. Remarkably, the dominance of hollow site adsorption for TCE and TCB tracks well with the proportion of standing adsorbates with the {110} substrate at the highest end followed by {100}, then by {111}. It should be recalled from the mass density profiling in Figure 1 and from the side view snapshots in Figure 2, the adsorbates reach the closest to the substrate when adsorbing on Pd {110}, which is permitted by hollow site adsorption. Interestingly, similar behavior is observed for the PCB77 case even though the PCB77 molecules are preferentially lying flat on all the three Pd facets.

Adsorption on atop sites, in contrast, is minimal for all facets except for PCB77 on {100}, almost disappearing in the case of TCB molecules adsorbed on the {110} facet (0.03% of total adsorbed content). For PCB77, the atop-adsorbed population size exceeds that of TCB and TCE due to the higher tendency of face-flat adsorbed PCB77 molecules to cross over multiple hollow and bridge sites and be anchored to atop sites (Figure 10). It is instructive to note the catalytic significance of Pd atom density in the case of the {100} surface that seems to play a significant role in PCB77's atop adsorptive performance (Figure 10C) relative to the behavior of TCE and TCB. The superior photocatalytic dichlorination efficiency of such surface configuration was recently reported for biphenyl surface retention, particularly for PCB77 (Guo et al., 2022).

Furthermore, for the case of TCE and TCB, atop adsorption is found to be quite distinct from hollow and bridge adsorptions both energetically and conformationally. Energetically, these sites see the highest per-molecule surface affinity on the {110} facet (grey line plots in Figure 10) and provides more active site of chloride for reaction. This matches a predominantly face flat orientation (small orientation angles) compared to the other two site types (orientation angles generally more extensive than 45 degrees), as shown by the representative angle decomposition in Figure 11, which further clarifies that the dominantly perpendicular orientation on the {110} facet for TCE and TCB reported above based on Figure 3 is due to the predominantly perpendicular orientation of the molecules on the bridge and hollow sites. For small molecules like TCE, the organic molecules tend to obey standing geometry on hollow sites to maximize the active chloride atoms. While for large molecular size, the standing geometry is less energy favorable which leads to a larger population of atop type.

Because of the much bigger size of PCB77 molecules compared with the separation distance between the Pd facet adsorption sites, many of the interfacial PCB77 molecules can be considered adsorbed on more than one adsorption site. The large error bars for the binding energy values in Figure 10C reflect that conclusion. The focus in interpreting the data in Figure 10C should be on the trend, not the absolute values. The mechanism of dechlorination reaction could also be changed by varieties of organics molecule orientation. Dedicated sites and corresponding activation energy should be carefully addressed in determining catalytic activity for COCs removal for molecules with large size and volume.

4 Conclusion

In conclusion, the molecular packing, templated ordering, energy preference, differential mobility for TCE, TCB and PCB77 on Pd surfaces point to a facet-dependent behavior that could be optimized for organic remediation.

The packing of TCE and TCB molecules on the Pd {110} surface shows a steric-influenced dynamic equilibrium that leads to interdigitated chain conformations. Along with a weak templating effect (Wandelt and Hulse, 1984; Dong et al., 1998) from the more corrugated Pd {110} surface, this surface is markedly different from the {100} and {111} surfaces. These Adsorbates were found to attain a standing formation most likely and to reach into hollow sites on Pd {110} surfaces compared to Pd {111} and Pd {100} counterparts. The interdigitated nature of adsorption on the Pd {110} is further manifested by a lack of clear surface structure relative to the other two facets, as seen by surface radial distribution functions. This packing and site-specific behavior were observed to set the stage for an exciting interplay between interdigitation and face-flat orientation during the adsorption process. Unlike the two small adsorbates, the packing of PCB77 molecules shows less dependence on the Pd facet type because of their relatively large molecular size and are observed to lay parallel to the Pd surface preferentially.

The per-molecule adsorption affinity is correlated to the proportion of face-flat adsorbates (Pd $\{111\}$ > Pd $\{100\}$ > Pd $\{110\}$). The surface area utilization of adsorbates, dictated by the per-area group energy, is enhanced when molecules either attain majority face-flat conformation (on Pd $\{111\}$) or when sufficient

interdigitation occurs due to a grander number of interspersed standing adsorbates (on Pd {110}) and thus results the more informative affinity of Pd {110} > Pd {111} > Pd {100}. TCE and TCB molecules have reduced mobility near the adsorption region, although the latter tend to reside longer than their TCE counterparts. The mobility of PCB77 molecules near the adsorption region within the time window of the current simulation time is extremely slow compared with the mobility of TCE and TCB. Importantly, the awayfrom-the-surface diffusion is well suppressed on all substrates and for all adsorbing species. The effect of adsorbate size, especially regarding aromatic core size, was evident in the distinctly planar adsorption of PCB77. This is in keeping with the enhanced short-range molecule substrate attraction driven by aromatic ring multiplicity on other nano surfaces reported elsewhere (Li et al., 2019). The hydrodechlorination reaction mechanism would be divergent for varieties of molecular orientation of different adsorption sites on each facet. The Pd facet preference for containment removal should be concluded on a caseby-case basis taking activation energy, molecular geometry, reactive chloride atoms, adsorption site and facets into account. The results reported in this work proposed some limitations of traditional DFT calculations. The similarity and discrepancy between our MD simulations and DFT calculations bring refreshing insight into the necessity of applying QM/MM simulations to the research of catalytic removal of COCs from the microscopic view.

Such palladium adsorption preference effects have already been utilized in nano-catalysis for targeted therapeutics in cancer treatment and in increasing the yield from coupling reactions (Long et al., 2013; Wang et al., 2013; Wang et al., 2014) but are under-utilized for organic remediation. Based on our analysis, differences in size and facet distribution can be optimized in a matrix-based system to utilize the maximum contaminant retention efficiency of Pd nanoparticles. It should be noted that adsorption of mixtures of organics at varied desired concentrations may lead to additional design factors such as effects from hydration and interfacial displacement, as well as competitive adsorption, and will be the focus of the future investigation. Signatures from the adsorption profiles presented here provide features for high throughput optimization of catalytic and remediation systems.

Data availability statement

The raw data supporting the conclusions of this article will be made available by the authors, without undue reservation.

Author contributions

HG and EG performed the simulations. HG, EG, IA, and MT were involved in post-processing of the data, analysis, and writing. KJ, IA, MH, TK, and MT were involved in guidance.

Funding

Support is acknowledged from Department of Energy that has allowed broad academic collaboration in high throughput catalytic discovery for industrial applications. IA and MT also acknowledge NSF support through grant number CHE-1665284. The authors

declare that this study received funding from Biena Tech LLC through DOE STTR grant number DE-SC0018875. The funder advised the overall effort but the MT research group had complete academic independence in the study design, collection, analysis, interpretation of data, the writing of this article, and the decision to submit it for publication.

Conflict of interest

KJ is a founder of Biena Tech LLC. HG was employed by Biena Tech LLC.

The remaining authors declare that the research was conducted in the absence of any commercial or financial relationships that could be construed as a potential conflict of interest.

References

Bokare, V., Jung, J. L., Chang, Y. Y., and Chang, Y. S. (2013). Reductive dechlorination of octachlorodibenzo-p-dioxin by nanosized zero-valent zinc: Modeling of rate kinetics and congener profile. *J. Hazard. Mat.* 250–251, 397–402. doi:10.1016/j.jhazmat.2013.02.020

Brown, H. S., Bishop, D. R., and Rowan, C. A. (1984). The role of skin absorption as a route of exposure for volatile organic compounds (VOCs) in drinking water. *Am. J. Public Health* 74 (5), 479–484. doi:10.2105/AJPH.74.5.479

Chen, A., and Ostrom, C. (2015). Palladium-based nanomaterials: Synthesis and electrochemical applications. *Chem. Rev.* 115, 11999–12044. doi:10.1021/acs.chemrev.5b00324

Chen, Y. H., Hung, H. H., and Huang, M. H. (2009). Seed-mediated synthesis of palladium nanorods and branched nanocrystals and their use as recyclable suzuki coupling reaction catalysts. *J. Am. Chem. Soc.* 131 (25), 9114–9121. doi:10.1021/ja903305d

Cheong, S., Watt, J. D., and Tilley, R. D. (2010). Shape control of platinum and palladium nanoparticles for catalysis. *Nanoscale* 5, 2045–2053. doi:10.1039/c0nr00276c

Clark, C. J., Rao, P. S. C., and Annable, M. D. (2003). Degradation of perchloroethylene in cosolvent solutions by zero-valent iron. *J. Hazard. Mat.* 96 (1), 65–78. doi:10.1016/S0304-3894(02)00162-0

Domalski, E. S., and Hearing, E. D. (1996). Heat capacities and entropies of organic compounds in the condensed phase. Volume III. *J. Phys. Chem. Ref. Data* 25 (1), 1–525. doi:10.1063/1.555985

Dong, W., Ledentu, V., Sautet, P., Eichler, A., and Hafner, J. (1998). Hydrogen adsorption on palladium: A comparative theoretical study of different surfaces. *Surf. Sci.* 411 (1–2), 123–136. doi:10.1016/S0039-6028(98)00354-9

Drollette, B. D., Hoelzer, K., Warner, N. R., Darrah, T. H., Karatum, O., O'Connor, M. P., et al. (2015). Elevated levels of diesel range organic compounds in groundwater near marcellus gas operations are derived from surface activities. *Proc. Natl. Acad. Sci. U. S. A.* 112 (43), 13184–13189. doi:10.1073/pnas.1511474112

Enache, D. I., Edwards, J. K., Landon, P., Solsona-Espriu, B., Carley, A. F., Herzing, A. A., et al. (2006). Solvent-free oxidation of primary alcohols to aldehydes using Au-Pd/TiO $_2$ catalysts. $Sci.\ (80$ -.) 311 (5759), 362–365. doi:10.1126/science.1120560

Essaid, H. I., Bekins, B. A., and Cozzarelli, I. M. (2015). Organic contaminant transport and fate in the subsurface: Evolution of knowledge and understanding. *Water Resour. Res.* 51 (7), 4861–4902. doi:10.1002/2015WR017121

Guo, W., Guo, B., Chen, H., Liu, C., and Wu, L. (2022). Facet-engineering palladium nanocrystals for remarkable photocatalytic dechlorination of polychlorinated biphenyls. *Catal. Sci. Technol.* 12 (1), 192–200. doi:10.1039/d1cy01752g

Hagenmaler, H., Brunner, H., Haag, R., and Kraft, M. (1987). Copper-catalyzed dechlorination/hydrogenation of polychlorinated dibenzo-p-dioxins, polychlorinated dibenzofurans, and other chlorinated aromatic compounds. *Environ. Sci. Technol.* 21 (11), 1085–1088. doi:10.1021/es00164a007

He, F., Zhao, D., Liu, J., and Roberts, C. B. (2007). Stabilization of Fe - Pd nanoparticles with sodium carboxymethyl cellulose for enhanced transport and dechlorination of trichloroethylene in soil and groundwater. *Ind. Eng. Chem. Res.* 46 (1), 29–34. doi:10.1021/ie0610896

He, Z., Jian, Q., Tang, J., Xu, T., Xu, J., Yu, Z., et al. (2016). Improvement of electrochemical reductive dechlorination of 2,4-dichlorophenoxyacetic acid using palladium catalysts prepared by a pulsed electrodeposition method. *Electrochim. Acta* 222, 488–498. doi:10.1016/I.ELECTACTA.2016.11.001

Heinz, H., Lin, T. J. J., Kishore Mishra, R., and Emami, F. S. (2013). Thermodynamically consistent force fields for the assembly of inorganic, organic, and biological nanostructures: The INTERFACE force field. *Langmuir* 29 (6), 1754–1765. doi:10.1021/la3038846

Publisher's note

All claims expressed in this article are solely those of the authors and do not necessarily represent those of their affiliated organizations, or those of the publisher, the editors and the reviewers. Any product that may be evaluated in this article, or claim that may be made by its manufacturer, is not guaranteed or endorsed by the publisher.

Supplementary material

The Supplementary Material for this article can be found online at: https://www.frontiersin.org/articles/10.3389/fctls.2023.1116867/full#supplementary-material

Heinz, H., Vaia, R. A., Farmer, B. L., and Naik, R. R. (2008). Accurate simulation of surfaces and interfaces of face-centered cubic metals using 12-6 and 9-6 Lennard-Jones potentials. *J. Phys. Chem. C* 112 (44), 17281–17290. doi:10.1021/jp801931d

Hozalski, R. M., Zhang, L., and Arnold, W. A. (2001). Reduction of haloacetic acids by Fe0: Implications for treatment and fate. *Environ. Sci. Technol.* 35 (11), 2258–2263. doi:10.1021/es001785b

Huang, C. C., Lo, S. L., Tsai, S. M., and Lien, H. L. (2011). Catalytic hydrodechlorination of 1,2-dichloroethane using copper nanoparticles under reduction conditions of sodium borohydride. *J. Environ. Monit.* 13 (9), 2406–2412. doi:10.1039/c1em10370a

Ji, X., Lee, K. T., Holden, R., Zhang, L., Zhang, J., Botton, G. A., et al. (2010). Nanocrystalline intermetallics on mesoporous carbon for direct formic acid fuel cell anodes. *Nat. Chem.* 2 (4), 286–293. doi:10.1038/nchem.553

Jiang, G., Li, X., Shen, Y., Shi, X., Lv, X., Zhang, X., et al. (2020). Mechanistic insight into the electrocatalytic hydrodechlorination reaction on palladium by a facet effect study. J. Catal. 391, 414–423. doi:10.1016/J.JCAT.2020.09.008

Jorgensen, L., Maxwell, S., Tirado-Rives, J., Jorgensen, W. L., Maxwell, D. S., and Tirado-Rives (1996). Development and testing of the OPLS all-atom force field on conformational energetics and properties of organic liquids. *J. Am. Chem. Soc.* 118 (45), 11225–11236. doi:10.1021/ja9621760

Kanhaiya, K., Kim, S., Im, W., and Heinz, H. (2021). Accurate simulation of surfaces and interfaces of ten FCC metals and steel using lennard–jones potentials. *npj Comput. Mat.* 7 (1), 17. doi:10.1038/s41524-020-00478-1

Kim, Y. H., and Carraway, E. R. (2003). Dechlorination of chlorinated phenols by zero valent zinc. *Environ. Technol. (United Kingdom)* 24 (12), 1455–1463. doi:10.1080/09593330309385690

Leuty, G. M., and Tsige, M. (2011). Characterization of CF4/CF3Br binary mixture adsorption on hydrophobic/hydrophilic surfaces via atomistic MD simulation. *J. Phys. Chem. B* 115 (44), 12694–12708. doi:10.1021/jp2057139

Leuty, G. M., and Tsige, M. (2010). Structure and dynamics of tetrahalomethane adsorption on (001) surfaces of graphite and α -quartz. *J. Phys. Chem. B* 114 (44), 13970–13981. doi:10.1021/jp1065049

Leuty, G., Nehring, J., and Tsige, M. (2009). Structure of multilayers on (0001) surfaces of graphite and hydroxylated -quartz: A molecular dynamics study. *Surf. Sci.* 603 (23), 3374–3381. doi:10.1016/j.susc.2009.09.030

Li, S., Arsano, I., Talapatra, S., Tsige, M., and Ma, X. (2019). Adsorption of aromatic carboxylic acids on carbon nanotubes: Impact of surface functionalization, molecular size and structure. *Environ. Sci. Process. Impacts* 21 (12), 2109–2117. doi:10.1039/c9em00417c

Li, W., Ma, H., Huang, L., and Ding, Y. (2011). Well-defined nanoporous palladium for electrochemical reductive dechlorination. *Phys. Chem. Chem. Phys.* 13 (13), 5565–5568. doi:10.1039/c0cp02178d

Long, R., Mao, K., Ye, X., Yan, W., Huang, Y., Wang, J., et al. (2013). Surface facet of palladium nanocrystals: A key parameter to the activation of molecular oxygen for organic catalysis and cancer treatment. *J. Am. Chem. Soc.* 135 (8), 3200–3207. doi:10.1021/ja311739v

Lookman, R., Bastiaens, L., Borremans, B., Maesen, M., Gemoets, J., and Diels, L. (2004). Batch-test study on the dechlorination of 1,1,1-trichloroethane in contaminated aquifer material by zero-valent iron. *J. Contam. Hydrol.* 74 (1–4), 133–144. doi:10.1016/j.jconhyd.2004.02.007

Lou, Y. Y., Xiao, C., Fang, J., Sheng, T., Ji, L., Zheng, Q., et al. (2022). High activity of step sites on Pd nanocatalysts in electrocatalytic dechlorination. *Phys. Chem. Chem. Phys.* 24 (6), 3896–3904. doi:10.1039/d1cp04975e

Lowry, G. V., and Reinhard, M. (1999). Hydrodehalogenation of 1- to 3-carbon halogenated organic compounds in water using a palladium catalyst and hydrogen gas. *Environ. Sci. Technol.* 33 (11), 1905–1910. doi:10.1021/es980963m

Meena, S. K., and Sulpizi, M. (2016). From gold nanoseeds to nanorods: The microscopic origin of the anisotropic growth. *Angew. Chem. - Int. Ed.* 55 (39), 11960–11964. doi:10. 1002/anie.201604594

Mishra, K., Basavegowda, N., and Lee, Y. R. (2015). Biosynthesis of Fe, Pd, and Fe-Pd bimetallic nanoparticles and their application as recyclable catalysts for [3 + 2] cycloaddition reaction: A comparative approach. *Catal. Sci. Technol.* 5 (5), 2612–2621. doi:10.1039/c5cv00099h

Muftikian, R., Fernando, Q., and Korte, N. (1995). A method for the rapid dechlorination of low molecular weight chlorinated hydrocarbons in water. Water Res. $29~(10),\,2434-2439.\,$ doi:10.1016/0043-1354(95)00102-Q

Nizzetto, L., Lohmann, R., Gioia, R., Dachs, J., and Jones, K. C. (2010). Atlantic Ocean surface waters buffer declining atmospheric concentrations of persistent organic pollutants. *Environ. Sci. Technol.* 44 (18), 6978–6984. doi:10.1021/es101293v

Parbs, A., Ebert, M., and Dahmke, A. (2007). Long-term effects of dissolved carbonate species on the degradation of trichloroethylene by zerovalent iron. *Environ. Sci. Technol.* 41 (1), 291–296. doi:10.1021/es061397v

Pavloudis, T., Kioseoglou, J., and Palmer, R. E. (2022). An ab initio study of size-selected Pd nanocluster catalysts for the hydrogenation of 1-pentyne. *Phys. Chem. Chem. Phys.* 24 (5), 3231–3237. doi:10.1039/d1cp05470h

Plimpton, S. (1995). Fast parallel algorithms for short-range molecular dynamics. *J. Comput. Phys.* 117 (1), 1–19. doi:10.1006/jcph.1995.1039

Postigo, C., and Barceló, D. (2015). Synthetic organic compounds and their transformation products in groundwater: Occurrence, fate and mitigation. *Sci. Total Environ.* 503–504, 32–47. doi:10.1016/j.scitotenv.2014.06.019

Sharma, S., and Bhattacharya, A. (2017). Drinking water contamination and treatment techniques. *Appl. Water Sci.* 7 (3), 1043–1067. doi:10.1007/s13201-016-0455-7

Shenoy, C. S., Khan, T. S., Verma, K., Tsige, M., Jha, K. C., Haider, M. A., et al. (2021). Understanding the origin of structure sensitivity in hydrodechlorination of trichloroethylene on a palladium catalyst. *React. Chem. Eng.* 6 (12), 2270–2279. doi:10.1039/d1re00252j

Śrebowata, A., Tarach, K., Girman, V., and Góra-Marek, K. (2016). Catalytic removal of trichloroethylene from water over palladium loaded microporous and hierarchical zeolites. *Appl. Catal. B Environ.* 181, 550–560. doi:10.1016/j.apcatb.2015.08.025

Su, J., Lin, S., Chen, Z., Megharaj, M., and Naidu, R. (2011). Dechlorination of P-chlorophenol from aqueous solution using bentonite supported Fe/Pd nanoparticles: Synthesis, characterization and kinetics. *Desalination* 280 (1–3), 167–173. doi:10.1016/j. desal.2011.06.067

Tedsree, K., Li, T., Jones, S., Chan, C. W. A., Yu, K. M. K., Bagot, P. A. J., et al. (2011). Hydrogen production from formic acid decomposition at room temperature using a Ag-Pd core-shell nanocatalyst. *Nat. Nanotechnol.* 6 (5), 302–307. doi:10.1038/nnano. 2011 42

Van Der Linde, P. R., Van Miltenburg, J. C., Van Den Berg, G. J. K., and Oonk, H. A. J. (2005). Low-temperature heat capacities and derived thermodynamic functions of 1,4-

dichlorobenzene, 1,4-dibromobenzene, 1,3,5-trichlorobenzene, and 1,3,5-tribromobenzene. J. Chem. Eng. Data 50 (1), 164–172. doi:10.1021/je049762q

Vijwani, H., and Mukhopadhyay, S. M. (2012). Palladium nanoparticles on hierarchical carbon surfaces: A new architecture for robust nano-catalysts. *Appl. Surf. Sci.* 263, 712–721. doi:10.1016/j.apsusc.2012.09.146

Wandelt, K., and Hulse, J. E. (1984). Xenon adsorption on palladium. I. The homogeneous (110), (100), and (111) surfaces. *J. Chem. Phys.* 80, 1340–1352. doi:10. 1063/1.446815

Wang, F., Lu, Z., Yang, L., Zhang, Y., Tang, Q., Guo, Y., et al. (2013). Palladium nanoparticles with high energy facets as a key factor in dissociating O2 in the solvent-free selective oxidation of alcohols. *Chem. Commun.* 49 (59), 6626–6628. doi:10.1039/c3cc42674b

Wang, Q., Cui, X., Guan, W., Zhang, L., Fan, X., Shi, Z., et al. (2014). Shape-dependent catalytic activity of oxygen reduction reaction (ORR) on silver nanodecahedra and nanocubes. *J. Power Sources* 269, 152–157. doi:10.1016/j.jpowsour.2014.06.160

Wang, X., Wang, W., Lowry, G., Li, X., Guo, Y., and Li, T. (2018). Preparation of palladized carbon nanotubes encapsulated iron composites: Highly efficient dechlorination for trichloroethylene and low corrosion of nanoiron. *R. Soc. Open Sci.* 5 (6), 172242. doi:10.1098/rsos.172242

Wania, F., and Mackay, D. (1996). Peer reviewed: Tracking the distribution of persistent organic pollutants. *Environ. Sci. Technol.* 30, 390A–396A. doi:10.1021/es962399q

Warczinski, L., and Hättig, C. A. (2019). A quantum chemical study of hydrogen adsorption on carbon-supported palladium clusters. *Phys. Chem. Chem. Phys.* 21 (38), 21577–21587. doi:10.1039/c9cp04606b

Warczinski, L., and Hättig, C. (2020). Correction: A quantum chemical study of hydrogen adsorption on carbon-supported palladium clusters. *Phys. Chem. Chem. Phys.* 15, 8233–8234. doi:10.1039/d0cp90079f

Xie, X., Gao, G., Pan, Z., Wang, T., Meng, X., and Cai, L. (2014). Large-scale synthesis of palladium concave nanocubes with high-index facets for sustainable enhanced catalytic performance. *Sci. Rep.* 5, 8515. doi:10.1038/srep08515

Xu, J., and Bhattacharyya, D. (2007). Fe/Pd nanoparticle immobilization in microfiltration membrane pores: Synthesis, characterization, and application in the dechlorination of polychlorinated biphenyls. *Industrial Eng. Chem. Res. Chem. Soc.* 46, 2348–2359. doi:10.1021/ie0611498

Yang, C. W., Chanda, K., Lin, P. H., Wang, Y. N., Liao, C. W., and Huang, M. H. (2011). Fabrication of Au-Pd core-shell heterostructures with systematic shape evolution using octahedral nanocrystal cores and their catalytic activity. *J. Am. Chem. Soc.* 133 (49), 19993–20000. doi:10.1021/ja209121x

Zhang, W. X. (2003). Nanoscale iron particles for environmental remediation: An overview. *J. Nanoparticle Res.* 5, 323–332. doi:10.1023/A:1025520116015

Zhang, W. X., Wang, C. B., and Lien, H. L. (1998). Treatment of chlorinated organic contaminants with nanoscale bimetallic particles. *Catal. Today* 40 (4), 387–395. doi:10. 1016/S0920-5861(98)00067-4

Zheng, Y., and Allen, D. G. (1996). Biological dechlorination of model organochlorine compounds in bleached kraft mill effluents. *Environ. Sci. Technol.* 30 (6), 1890–1895. doi:10.1021/es950527p